Land subsidence in Beijing and its relationship with geological faults revealed by Sentinel-1 InSAR observations

Leyin Hu[a,b], Keren Dai[a,c*], Chengqi Xing[b], Zhenhong Li[d,e], Roberto Tomás[f],

Beth Clark[g], Xianlin Shi[a], Mi Chen[h], Rui Zhang[i], Qiang Qiu[j,k], Yajun Lu[l]

[a] College of Earth Sciences, Chengdu University of Technology, Chengdu 610059, China;

[b] Beijing Earthquake Agency, Beijing 100080, China;

[c] State Key Laboratory of Geohazard Prevention and Geoenviroment Protection, Chengdu University of Technology, Chengdu 610059, China;

[d] COMET, School of Engineering, Newcastle University, Newcastle upon Tyne NE1 7RU, UK;

[e] College of Geological Engineering and Geomatics, Chang'an University, Xi'an 710054, China

[f] Departamento de Ingeniería Civil, Escuela Politécnica Superior, Universidad de Alicante, P.O. Box 99, E-03080 Alicante, Spain

[g] School of Natural and Environmental Sciences, Newcastle University, Newcastle upon Tyne, NE1 7RU, UK

[h] College of Resources Environment and Tourism, Capital Normal University, Beijing 10048, China;

[i] Department of Remote Sensing and Geospatial Information Engineering, Southwest Jiaotong University, Chengdu 610031, China;

[j] Earth Observatory of Singapore, Nanyang Technological University, 639798 Singapore;

[k] Asian School of the Environment, Nanyang Technological University, 639798 Singapore;

[l] Changping Earthquake Monitoring Station of Beijing Earthquake Agency, Beijing 102209, China;

* Corresponding author. E-mail: daikeren17@cdut.edu.cn

Abstract: Beijing, the capital city of China, has been affected by land subsidence due to intensive groundwater extraction since 1935. Recent studies reported that the maximum subsidence occurred in the east of Beijing, reaching more than 11 cm/year till 2017. To investigate the subsidence (2015~2017) in Beijing, in this paper, time series interferometric synthetic aperture radar (TS-InSAR) analysis was performed with 22 Sentinel-1 Terrain Observation by Progressive Scans (TOPS) mode SAR data. Results show that wide areas in the east of Beijing are subsiding with a maximum rate of 14 cm/year, which is consistent with GPS data. Detailed analysis of the obtained subsidence map reveals the existence of several characteristic near-linear boundaries within the subsiding areas. As a result of our previous three-year project, we generated the exact location, direction, and late Quaternary activity of the main potential active faults in the Beijing area. The relationship between the trace of these existing geological faults and the mentioned subsidence boundaries was investigated in detail. It is suggested that land subsidence in Beijing was mainly caused by the over-extraction of groundwater, with its spatial pattern being controlled by geological faults.

Key words: InSAR; Sentinel-1 TOPS data; Beijing land subsidence; geological faults

1. Introduction

Beijing is the capital city of China and the political center of the country. It is located in northern China and has a population of more than 21 million. The Beijing region has been affected by land subsidence since 1935 (Xu et al. 2008). Previous studies showed that the main cause of land subsidence in this area is intensive groundwater extraction rather than other driving factors (Zhang et al., 2014). In fact, Xu et al. (2008) stated that two-third of drinking water and water supply for industries was withdrawn from the aquifer system, reaching an annual volume higher than 25×10^8 m^3. Recent studies reported that the most severe subsidence had been exhibiting in eastern Beijing, with a maximum subsistence rate of more than 10 cm/year (Chen et al., 2016; Zhou et al., 2017). Such widespread and rapid subsidence poses potential risks to high-rise buildings and urban infrastructure including subways and high-speed railways. Furthermore, Beijing is situated in an active tectonic zone with many active faults. Previous studies have analyzed the mechanisms of the subsidence and mentioned that the spatial subsidence pattern in Beijing is different from those in other places, e.g. the subsidence bowl pattern in Tianjin and Shanghai (Liang et al., 2013), indicating there might be some connections with these faults. Therefore, it is crucial to perform long-term, wide-coverage subsidence monitoring in Beijing to investigate the relationship between subsidence and these tectonic faults to enable a comprehensive understanding of potential geological hazards forecasting, subsidence mitigation strategies and fast emergency response.

Interferometric synthetic aperture radar (InSAR) technology has been proven a powerful tool to monitor wide-scale subsidence with high accuracy (Osmanoğlu et al., 2015; Crosetto et al., 2015), which has been successfully applied in city subsidence monitoring (e.g. Chen et al., 2016; Dai et al., 2015; Motagh et al., 2017). The land subsidence in Beijing between 2003 and 2017 was analyzed in detail based on InSAR with ALOS PALSAR, RADARSAT-2, Envisat ASAR, TerraSAR-X, ALOS PALSAR2 and Sentinel-1 SAR datasets in a number of previous studies (Table 1). Besides, subsidence-related factors were analyzed including groundwater over-exploitation, aquifer structure, crustal deformation, active faults, urban construction, land uses types, and soil thickness. According to these previous studies, land subsidence in the east of Beijing has existed for a long time (i.e. 2003~2017) with a relatively high rate (greater

than 10 cm/year). In order to investigate whether the subsidence rate was stable or not, continuous monitoring using InSAR with wide spatial coverage is ideal (e.g. Berger et al. 2012).

Table 1. Previous InSAR studies on land subsidence in Beijing.

Time span*	SAR data type	Studies	Factors analyzed
2003~2010	Envisat ASAR (C-band)	(Gong et al., 2009), (Ng et al., 2012), (Li et al., 2013), (Hu et al., 2014), (Zhu et al., 2015), (Chen et al., 2015) (Chen et al., 2016), (Chen et al., 2017), (Gao et al., 2018), (Zhou et al., 2018) (Yang et al. 2018)	Groundwater, aquifer structure, crustal deformation, active faults, urban construction land use types soil thickness
2007~2010	ALOS PALSAR (L-band)	(Ng et al., 2012), (Liang et al., 2013), (Du et al., 2018)	
2010-2015	RadarSAT-2 (C-band)	(Deng et al., 2017), (Zhou et al., 2018), (Chen et al, 2019)	
2010~2015	TerraSAR-X (X-band)	(Chen et al., 2016), (Zhou et al., 2017), (Deng et al., 2017), (Gao et al., 2018), (Zhou et al., 2018), (Yang et al. 2018) (Luo et al. 2018)	
2014-2017	ALOS PALSAR2 (L-band)	(Du et al., 2018)	
2014-2016	Sentinel-1 (C-band)	(Marinkovic et al., 2016), (Du et al., 2018)	
2015-2017	**Sentinel-1 (C-band)**	**This study**	**Geological faults**

* Some research only used the images in part of this time span.

In this paper, land subsidence in Beijing is investigated using an InSAR time series, consisting of 22 Sentinel-1A TOPS Interferometric Wide Swath (IW) images collected during the period between July 2015 and April 2017. The present land subsidence status in Beijing (from 2015 to 2017) is presented and validated by GPS data. With the assistance of optical images, the subsidence areas are analyzed in detail by connecting them to the land use. In addition, the location, direction, late Quaternary activity of the

main potential active faults in Beijing were precisely determined from our three-year project. Hence, possible links between the subsidence distribution, and the adjacent geological faults are explored and discussed.

2. Study area and datasets

2.1 The geological setting of Beijing
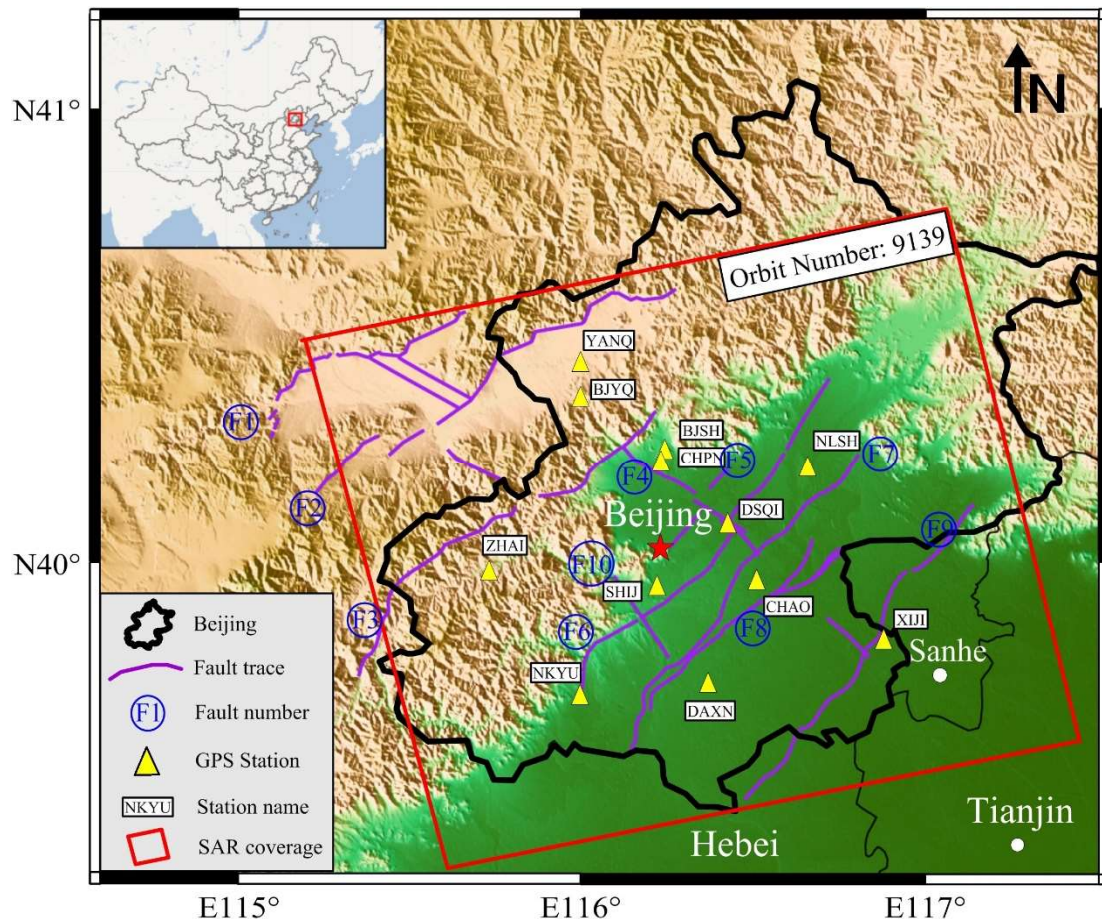
Fig. 1. Location of Beijing, main faults, GPS stations and the coverage of SAR data.

Beijing is located in the northern part of the North China plain, which is in the faults junction region between the faults system in Yanshan, North China Plain and Taihang Mountain. This junction region is one of the regions with strong seismic activity in China's history. Due to the complex tectonic setting of this junction region, the neotectonic movements are active, resulting in many active fault lines. These faults strike mainly in northeast (NE) and northwest (NW) direction, with 10 of them going directly through the city of Beijing. Most of these are normal faults, although some also present a strike-slip component. The faults play key roles in controlling the geological structural development of the basin rifting and depression in this region. Regarding the characteristics of the neotectonic movements, Beijing and its surrounding area can be

divided into four different tectonic regions that are the Beijing plain depression region, the Yanhui basin depression area, the western and northern Beijing mountain belts region (Deng et al., 2003). Key characteristics of these faults through Beijing are listed in Table 2.

Table 2. The characteristics of the main faults in Beijing area, based on our technical report (described in detail in section 2.2) and Xu et al. (2002). Q_2, Q_3 and Q_4 means the Middle Pleistocene, Late Pleistocene and Holocene, respectively. R: right-lateral, L: left-lateral. See Fig 1 for a map of the fault locations.

Fault ID and Fault name					
	Length (km)	Fault strike	Fault property	Active time	Mean slip rate (mm/year)
F1 Northern boundary fault of Huaizhuo Basin					
	58	NE	Normal fault	1720	0.29~0.55
F2 Northern boundary fault of Yanfan Basin					
	102	NE	Normal fault	1484	0.17~0.44
F3 Nankou Piedmont fault					
	60	NE	Normal fault	Q_3	0.1
F4 Nankou-Sunhe fault					
	60	NW	Normal fault (L)	Q_4	0.3
F5 Xiaotangshan-Dongbeiwang fault					
	24	NNE	Normal fault	Q_3	0.02~0.04
F6 Huangzhuang-Gaoliying fault					
	130	NNE	Normal fault	Q_4	0.1~0.2
F7 Shunyi-Liangxiang fault					
	100	NNE	Normal fault (R)	Q_{3-4}	0.15
F8 Tongxian-Nanyuan fault					
	60	NNE	Normal fault	Q_3	0.75
F9 Xiadian fault					
	120	NE	Normal fault (R)	Q_4	0.3~0.76
F10 Yongding River fault					
	26	NW	Normal fault (L)	Q_2	/

Specifically, the Beijing plain is located at the junction area between the North China plain depression region and the Zhangjiakou-Bohai tectonic belt, which is mainly controlled by the NE and NW direction active faults. The NE fault systems are composed mainly by the Nankou Mountain (F3), Xiaotang Mountain (F5), Huangzhuang-Gaoliying (F6), Shunyi-Liangxiang (F7), Tongxian-Nanyuan (F8), and Xiadian (F9) faults. The NW fault systems are composed mainly by the Nankou-Sunhe

(F4) and the Yongding River (F10) faults. These faults have been active over different time periods of the Quaternary time scale (see Table 2). Among these faults, those that are located in the northern and eastern part of the plain were activate in late Pleistocene age. The junction region of these two different striking fault systems is the most seismically active region, resulting in broad blind depression, e.g., Shahe, Shunyi and Dachang depression, with the maximum subsidence exceeding 500 meters since the Quaternary (Xu et al., 2002).

2.2 Datasets used in this study

The fault data used in this study was derived from a technical report of our recent three years project titled "*Active fault detection and seismic risk assessment in Beijing*" which was implemented during 2004 to 2007 by the Institute of Geology China Earthquake Administration and Beijing Earthquake Agency. In that project, the exact location, geometry, late Quaternary activity of the main active faults were determined using a range of methods such as regional physical exploration, seismic geological survey, drilling detection, Quaternary stratigraphic division, seismic accurate positioning and trench excavation and test.

The SAR images were acquired by Sentinel-1, which is a two-satellite constellation, i.e. Sentinel-1A and Sentinel-1B (ESA, 2018a). As the continuity of ESA's previous European Remote Sensing (ERS) and ENVISAT SAR missions, it provides C-band SAR data with further enhancements in terms of repeat cycle, coverage etc.. The Sentinel-1 satellites are able to map the global landmasses once every 6-24 days based on the acquisition plan at different places. Compared to the previous SAR data used for monitoring Beijing land subsidence (i.e. Envisat-ASAR, TerraSAR-X and ALOS-PALSAR), Sentinel-1 SAR data sets used in this study were acquired by the novel Interferometric Wide swath (IW) TOPS mode, with a total swath width of 250 km and spatial ground resolution of 20 x 5 m (Geudtner et al. 2016).
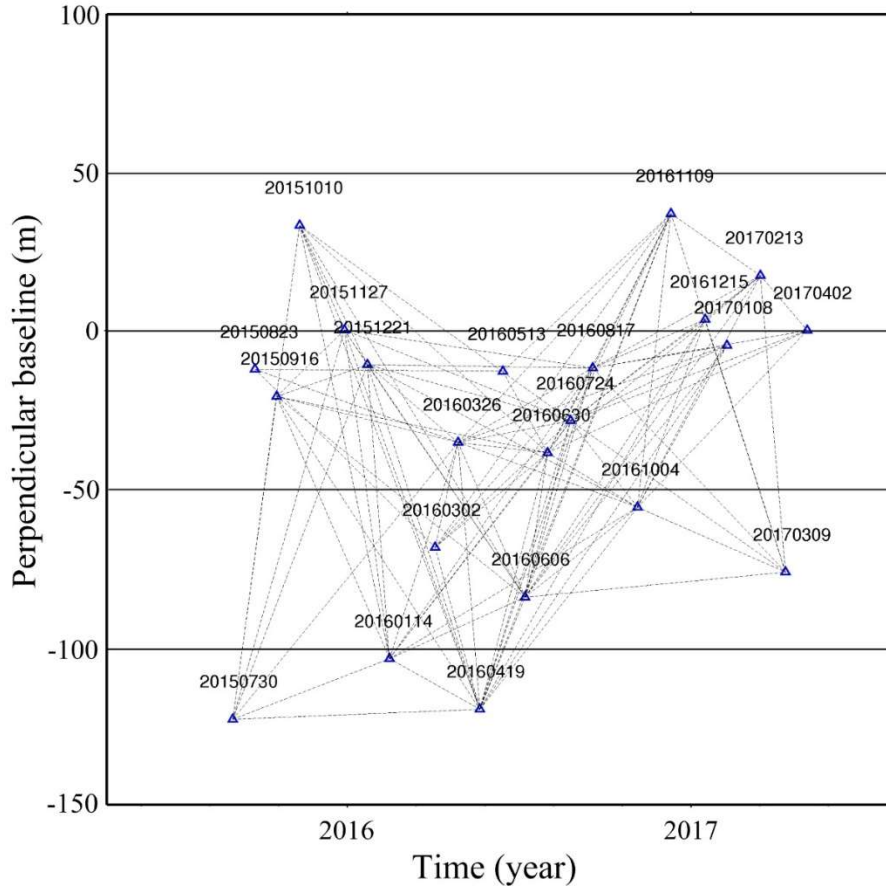
Fig. 2. Spatial and temporal baselines of the Sentinel-1 data used in this study.

As shown in Fig. 2, 22 ascending Sentinel-1A images in the IW TOPS mode have been collected from July 30th 2015 to April 2nd 2017 in this study. The blue triangles denote the time of SAR acquisition. The range and azimuth pixel spacings of this data sets are 2.33 m and 13.93 m respectively. At the step of interferogram generation, a multi-look factor of 5 (in range):1 (in azimuth) was applied, resulting in near square-sized ground pixels in the interferograms with the range and azimuth pixel spacings of 11.65 m and 13.93 m, respectively. The orbit maintenance strategy of the Sentinel-1 satellite ensures a ground-track repeatability of 120 m resulting in small orbital InSAR baselines on the order of 150 m (Yague et al., 2016). Considering the fact that the short InSAR baselines, the impacts of DEM errors on InSAR observations can be neglected. In addition, short baselines cause a negligible range spectral decorrelation, which is a pre-condition for achieving high coherence values close to 1. Therefore, the temporal and spatial baseline thresholds (i.e. 300 days and 150 m, respectively) were set to select interferometric pairs with potential high coherence, in which the phase unwrapping can be performed correctly. It should be noted that from July 30th 2015 to August 2016, there were only acquisitions every 24 days. After that the revisiting period was

improved to 12 days. In this study, the 22 acquisitions were selected with a fixed interval of 24 days based on (i) the study area was in Beijing urban area and, therefore, high coherence were acquired with even 97 days. (ii) 108 interferometric pairs were generated (shown with dash line in Fig. 2), which is enough to ensure sufficient redundant observation for the time series calculation.

3 Methodology

We investigate the present subsidence in the Beijing area using the TS InSAR + AEM (atmospheric estimation model) time series analysis approach (Li et al., 2009) on Sentinel-1 TOPS data sets. Fig. 3 presents the whole processing chain, which can be divided into four parts, i.e. data insertion, co-registration, interferometry and time-series analysis.
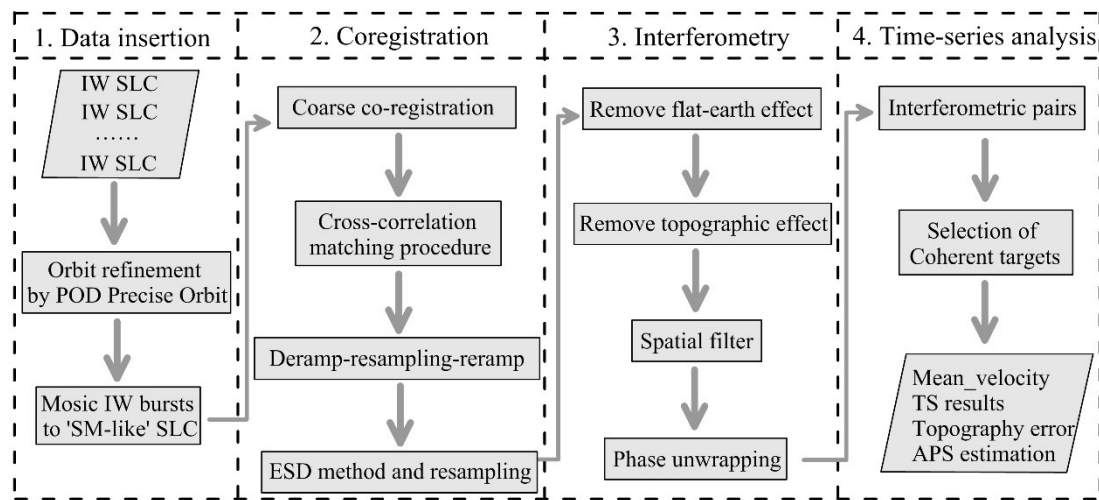
Fig. 3. Flowchart of the whole processing chain.

Firstly, as shown in Fig. 3 (part 1 – data insertion), the IW mode SLC (Single look complex) data is collected as the input data, which preserved phase information and are processed at the natural pixel spacing (ESA, 2018b). The Precise Orbit Determination (POD) data was used to help mosaic the data into 'normal SLC' (i.e. the matrixes contain amplitude and phase information in single look complex format). In part 2 (co-registration), a coarse image co-registration is performed considering the terrain height and orbit geometry, i.e. based upon orbital state vectors. Then we use an iterative co-registration method (Dai et al., 2016) to meet the stringent co-registration requirement of TOPS data, i.e. in azimuth direction a co-registration accuracy of 0.001 SLC pixel is required to reduce the phase jumps at the burst interface to 3 degree (Prats et al. 2010). This method uses cross-correlation matching and enhanced spectral diversity (ESD) methods (Scheiber et al. 2000) iteratively to refine the slight offset remained in coarse

co-registration and a very high level of azimuth co-registration accuracy was achieved (below 0.005 pixel). This method were performed on all bursts in three sub-swaths. As a result, all the bursts are synchronized and concatenated as one normal StripMap (SM)-like SLC for following steps, which means that the gaps, resulting from the ScanSAR-type burst imaging, are removed.

The Shuttle Radar Topography Mission (SRTM) digital elevation model (DEM) was used to remove the topographic phase and for the subsequent geocoding step. After we obtain the interferograms with 5 (in range):1 (in azimuth) multi-look factor for each pair, the adapted Goldstein filter (Goldstein and Werner, 1998) was applied to reduce the noise. Phase unwrapping was performed in two-dimensional space by the minimum cost flow (MCF) method (Chen and Zebker, 2002) with a coherence-based mask. Thus, we obtained unwrapped interferograms to form the baseline network as shown in Fig. 2. In this study, the processing steps, such as data insertion, image co-registration and interferomogram generation, was completed using commercial GAMMA software (GAMMA, 2018).

Based on these 108 unwrapped interferograms, the TS InSAR + AEM method was performed in the InSAR time series analysis, which integrates the atmospheric estimation model (AEM) into the conventional small baseline subset Interferometric Synthetic Aperture Radar (SBAS InSAR) analysis. In this method, the unwrapped phase for an arbitrary coherent pixel (x,y) in interferogram i (computed from SAR acquisitions at time t_1 and time t_2) can be modeled as,

$$\Delta \phi_i = \Delta \phi_{disp} + \Delta \phi_{topo} + \Delta \phi_{atm} \tag{1}$$

where ϕ_{disp}, ϕ_{topo} and ϕ_{atm} denote the phase components caused by land deformation, topographic error, atmospheric artifacts and decorrelation/thermal noise, respectively. Atmospheric artifacts are mainly due to the spatio-temporal changes (mainly caused by the atmospheric pressure, temperature and water vapor) in the refractive index of the medium, particularly the part due to water vapour (e.g. Li et al., 2005, 2006; Ding et al. 2008; Yu et al., 2017, 2018). For a given pixel in the temporal analysis, they can be expressed as,

$$\Delta\phi_{disp} = \frac{4\pi}{\lambda} \begin{bmatrix} t_2-t_1, t_2-t_1, & 0, & \cdots, & 0 \\ 0, & t_3-t_2, & t_4-t_3, & \cdots, 0 \\ \vdots & \vdots & \vdots & \vdots & \vdots \\ 0,0, & \cdots, t_n-t_{n-1}, & t_{n+1}-t_n \end{bmatrix} \begin{bmatrix} v_1 \\ v_2 \\ v_3 \\ \vdots \\ v_n \end{bmatrix} = TV \tag{2}$$

$$\Delta\phi_{topo} = \left[\frac{B_{\perp 1}}{r\sin\theta}, \frac{B_{\perp 2}}{r\sin\theta}, \cdots, \frac{B_{\perp 3}}{r\sin\theta} \right]^T \Delta Z = CZ \tag{3}$$

$$\Delta\phi_{atm} = AD, A = \begin{cases} 0, & (t_M \neq t_{APS} \text{ and } t_S \neq t_{APS}) \\ -1, & (t_M = t_{APS} \text{ and } t_S \neq t_{APS}) \\ +1, & (t_M \neq t_{APS} \text{ and } t_S = t_{APS}) \end{cases} \tag{4}$$

where λ, θ and v_n demotes the wavelength, incidence angle and deformation velocity during the corresponding time span, respectively. ΔZ is the topographic error caused by the inaccuracy of the DEM used in the interferometric processing. D is the atmospheric phase screen (APS) variable for the specific date t_{APS}. t_M and t_S denote the master and slave images for one interferogram, while coefficient vector A is expressed in equation (4). If a temporal deformation model is known, i.e.,

$$V = L \times P \tag{5}$$

where vector P contains p model parameters (typically less than four) (Li et al. (2009)) and L is the model matrix describing the velocity vector V. Combining the equations above, the final equation would be,

$$\begin{bmatrix} TL & C & A \\ M\times p & M\times 1 & M\times 1 \end{bmatrix} \begin{bmatrix} P \\ {}_{p\times 1} \\ Z \\ {}_{1\times 1} \\ D \\ {}_{1\times 1} \end{bmatrix} = \begin{bmatrix} R \\ M\times 1 \end{bmatrix} \tag{6}$$

It should be noted that in some cases the temporal deformation model is unknow and the temporal pattern of deformation is one of the aims. We could solve each v_n directly or with some simple model such as linear velocity (TLV) model. If all the acquisitions are well connected, which means they belong to a single subnetwork, we should have an overdetermined system with enough observations. The solution can be obtained in a least squares sense. The details on this time series method can be found in Li et al. (2009), Dai et al. (2016) and Zhou et al. (2016).

4 Subsidence results and analysis

4.1 Subsidence distribution map.
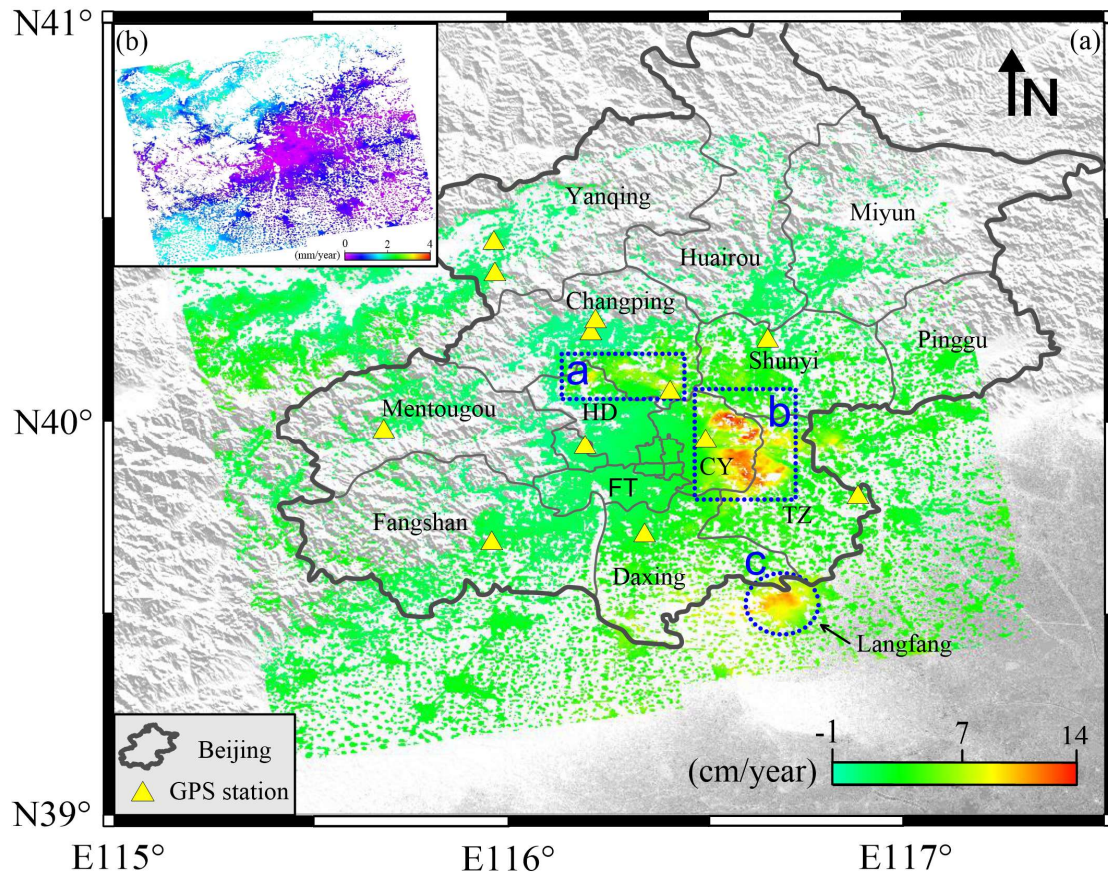
Fig. 4. (a) Mean velocity map of city subsidence in Beijing. (HD: Haidian district; CY: Chaoyang district; FT: Fengtai district; TZ: Tongzhou district). The positive value in the mean velocity map means the surface is moving away from the sensors. (b) The error map (RMS) of the mean velocity results.

The mean subsidence velocity map of Beijing was generated (Fig. 4a) using the Sentinel-1 data sets and by applying the InSAR time series method as mentioned previously. According to previous studies (e.g. Yang et al. 2003) and our GPS monitoring data from the period 2006-2010, the horizontal displacements in Beijing area were 1 mm/year along east-west direction and 0.7 mm/year along north-south direction. Therefore, vertical displacements are much higher than horizontal constituting the main component of ground displacements. Consequently, considering the flat topography of the basin in this study, the displacements acquired from InSAR (along the LOS direction) were directly interpreted as vertical in this study. As shown in Fig. 4a, the maximum subsidence rate is observed in eastern Beijing, revealing the most severe subsidence area in the east of Chaoyang District and the north of Tongzhou

District, with rates of up to 14 cm/year (rectangle b in Fig. 4a). In the north of Shunyi District, the subsidence rate reduces to less than 5 cm/year. In the northwest of Changping District and north of Haidian District, there is another subsidence area exhibiting a subsidence rate of 5-10 cm/year (see rectangle a in Fig. 4a). Except for these mentioned areas, the rest of the city of Beijing exhibits relatively stable behavior. It should be noted that, in the east corner of Daxing District, there is a subsidence area corresponding to the city of Langfang (see circle c in Fig. 4a), which is very close to the Beijing boundary. This result reveals that the subsidence of more than 10 cm/year has continued for over 10 years, meaning that the subsidence has not been controlled as of 2017. The error map (root mean square, RMS) of the mean velocity results was presented in Fig. 4b. It can be seen that the city center of Beijing and more specifically the areas studied in detail exhibit very low RMS while in the northwest and southwest zones of the study area the RMS increases up to 2 mm/yr with a mean of 0.8 mm/yr. This is mainly because of greater atmospheric effects in mountain areas than flat areas. The mean value of the RMS map was 0.791, which was very low for InSAR time series results.

4.2 Validation of results

In the study area, several continuous GPS stations were established during the period from 2006 to 2010. All these GPS stations are equipped with Trimble Net R8/R9 GNSS receivers and dual frequency observations. The continuous GPS observation signals were received since the establishment of the systems until the present day. We selected 12 GPS stations within the study area to carry out precise position solving to acquire subsistence movement in the up-down direction for the purpose of cross-validation with the rates obtained from InSAR measurements. The RINEX GPS observation files were processed with the GAMIT/GLOBK 10.6 software package from Massachusetts Institute of Technology (MIT), Scripps Institution of Oceanography and Harvard University. Satellite orbit and clock parameters were provided by International GNSS Service (IGS). The locations of the 12 GPS stations were shown in Fig. 1.
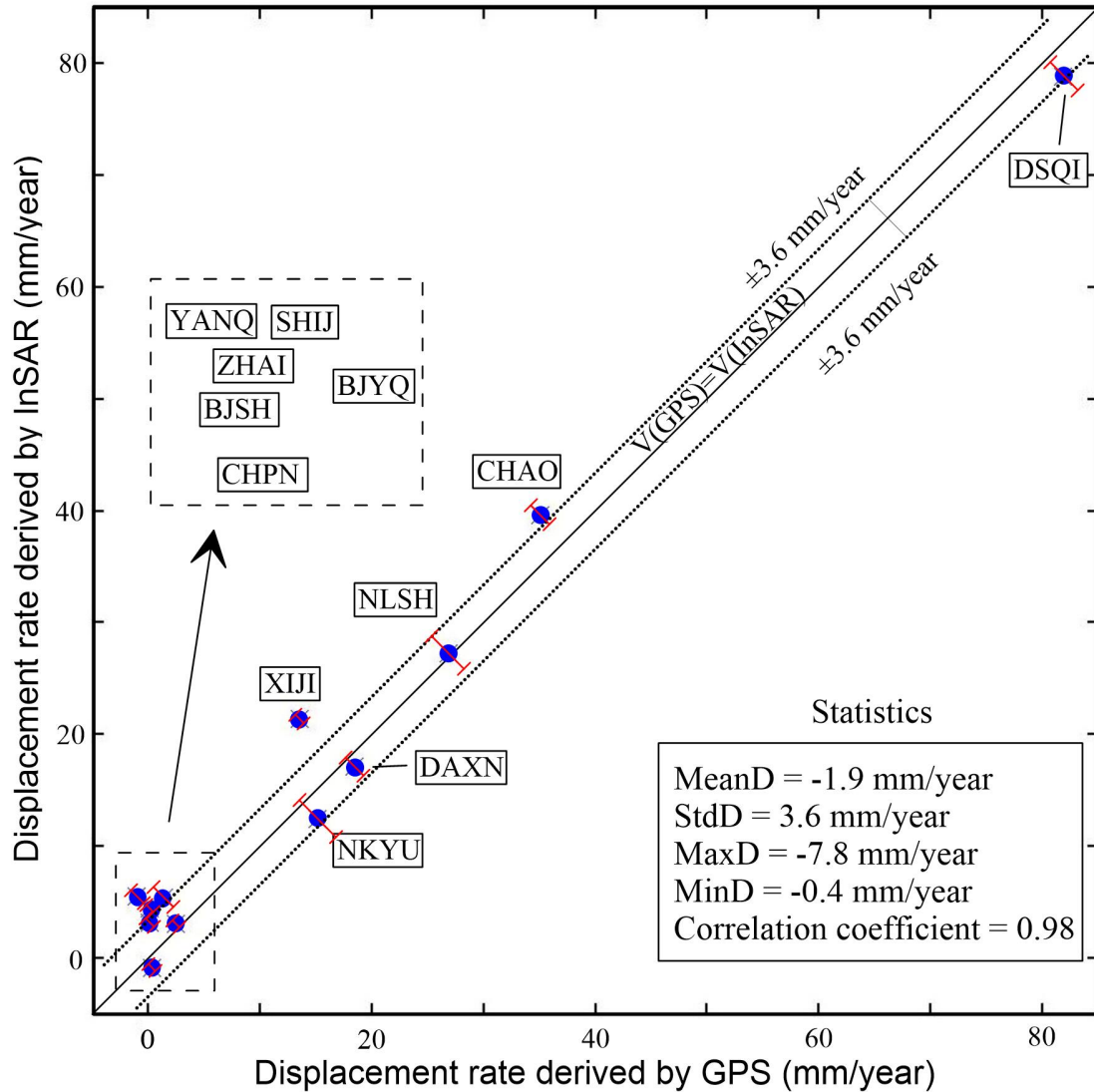
Fig. 5. Comparison between GPS and InSAR results. The red line denotes the error bar at each station. The locations of GPS stations are shown in Fig. 1.

The mean subsidence velocities measured at the 12 GPS stations (during the same time span as Sentinel-1 data) were acquired and projected onto the line of sight (LOS) direction of the satellite (i.e. multiply by the cosine of the radar incidence angle). For the GPS measurements uncertainties, we estimated the rates of motion from GPS vertical component time series and the rates uncertainties using the HECTOR software (BOS, 2013). The error in converting the GPS measurements into radar LOS values depends on the satellite orbit accuracy. Specifically, owing to uncertainty in satellite orbits, the InSAR LOS rate maps contain an error in their longest wavelength component (Hanssen, 2001). In this case, the Precise orbit ephemerides (POD) data provided by Sentinel-1 quality control subsystem were used to reduce the error from satellite orbits as much as possible, in which the position accuracy threshold is 5 cm 3D 1-sigma RMS for S-1 POE orbit files (GMV, 2017). Based on SAR geometry, the

uncertainties in the 3D GPS displacements can be projected in the radar line of sight and are shown in Fig. 5. The comparison between GPS and InSAR results are shown in Fig. 5. For the 12 GPS data points, the mean and standard deviation of the difference between measurements at each station and InSAR results are -1.9 mm/year and 3.6 mm/year, respectively, suggesting a good agreement between them. The correlation coefficient between GPS and InSAR results on these points is 0.98, showing the high accuracy of the InSAR mean velocity map. The maximum difference appeared on XIJI station, which is located near the east boundary of Beijing. The DSQI station is the closest one to the subsidence bowl exhibiting the maximum subsidence rate of the GPS stations, at 8 cm/year.

The mean velocity map was compared with previous studies (e.g. Chen et al. 2016; Deng et al., 2017; Gao et al. 2018; Chen et al. 2019), showing good agreements in the delimitation of the boundaries of the subsidence bowls. The large number of interferograms (108 in total), the high coherence in Beijing urban area and the dense distribution of coherent points and the sufficient redundant observations for InSAR time series analysis ensured the reliability of the results.

4.3 Analysis of the main subsiding areas

There is a well built in 1986 in the DSQI earthquake station, in Changping district with a subsidence rate of 5-10 cm/year (Rectangle a in Fig. 4). This well is used for detecting earthquake precursors including water level, water temperature and volumetric strain observations. A metal casing, consisting of a large diameter pipe that is assembled and inserted into a section of a borehole was installed when the well was drilled. The tip of this casing is embedded in a stable basement rock from the dolomite limestone of Sinian system, at a depth of 320 m. Above the ground surface, a part of this casing was exposed as shown in Fig. 6. Fig. 6a and 7b are photos of the exposed casing which were taken at 2006 and 2011, respectively. In 2011 the exposed part is clearly higher than it was in 2006 due to the subsidence of the ground (since the casing is stable, and so used as a reference point). In 2017, as shown in Fig. 6c, we measured the exposed part of the casing that have reached 80 cm. Although we do not have its quantitative height measurements in 2006 and 2011, we can infer from the photos that the height of the exposed casing was emerging from ground surface at a dramatic acceleration. The increment during 2011 to 2017 (in 6 years) was much more than that during 1986 to 2011 (in 15 years), indicating that from 2006, the subsidence rate in this

area has accelerated, and this rate as increased since 2011. The DSQI GPS station is about 50 m away from this building and records a subsidence rate of 8 cm/year.

The highest rates of land subsidence occur in the Beijing Plain located in the east of Chaoyang District and the north of Tongzhou District (Fig. 4). This area shows three main subsidence bowls that are depicted in Fig. 7a, namely Jinzhan, Magezhuang, Guanzhuang-Heizhuanghu. These places all suffer subsidence with a rate higher than 10 cm/year, while the Jinzhan area is the most severe place with a maximum subsidence rate of nearly 14 cm/year.
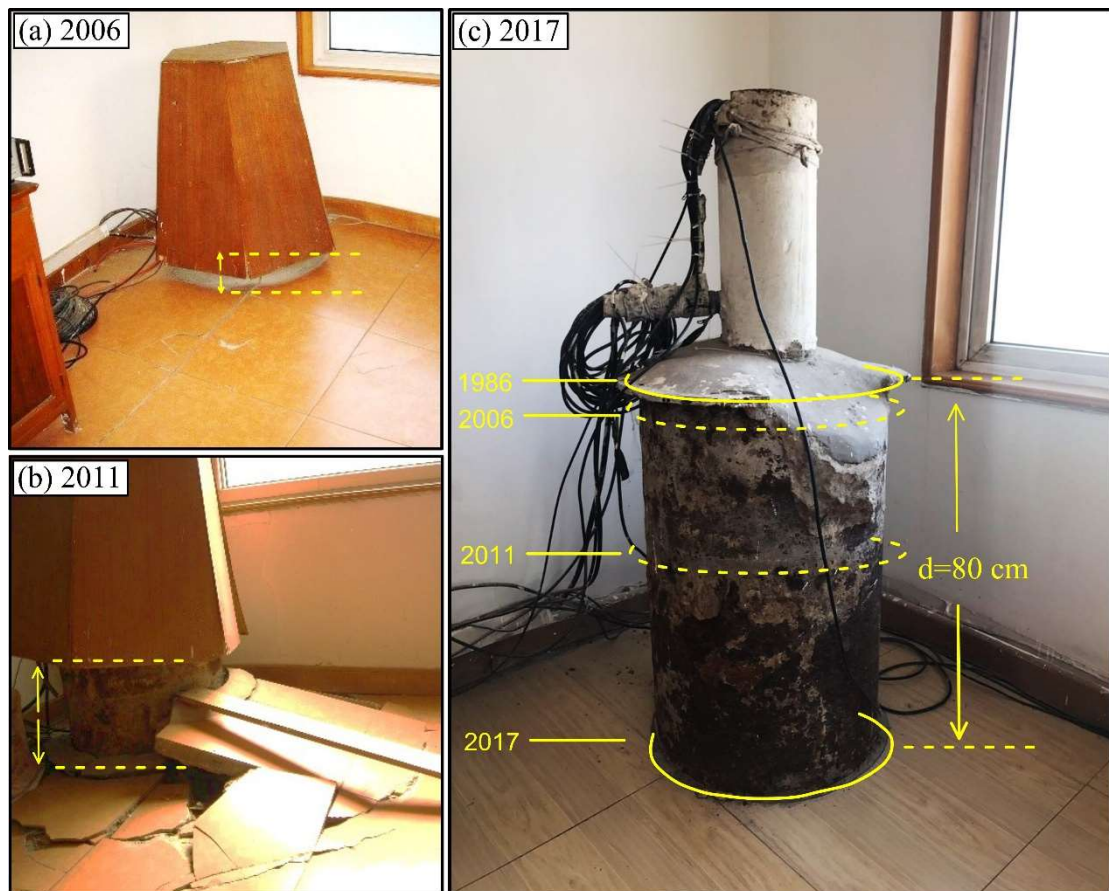
Fig. 6. Three photos of an exposed metal casing in DSQI earthquake station, taken on 2006, 2011 and 2017, respectively.
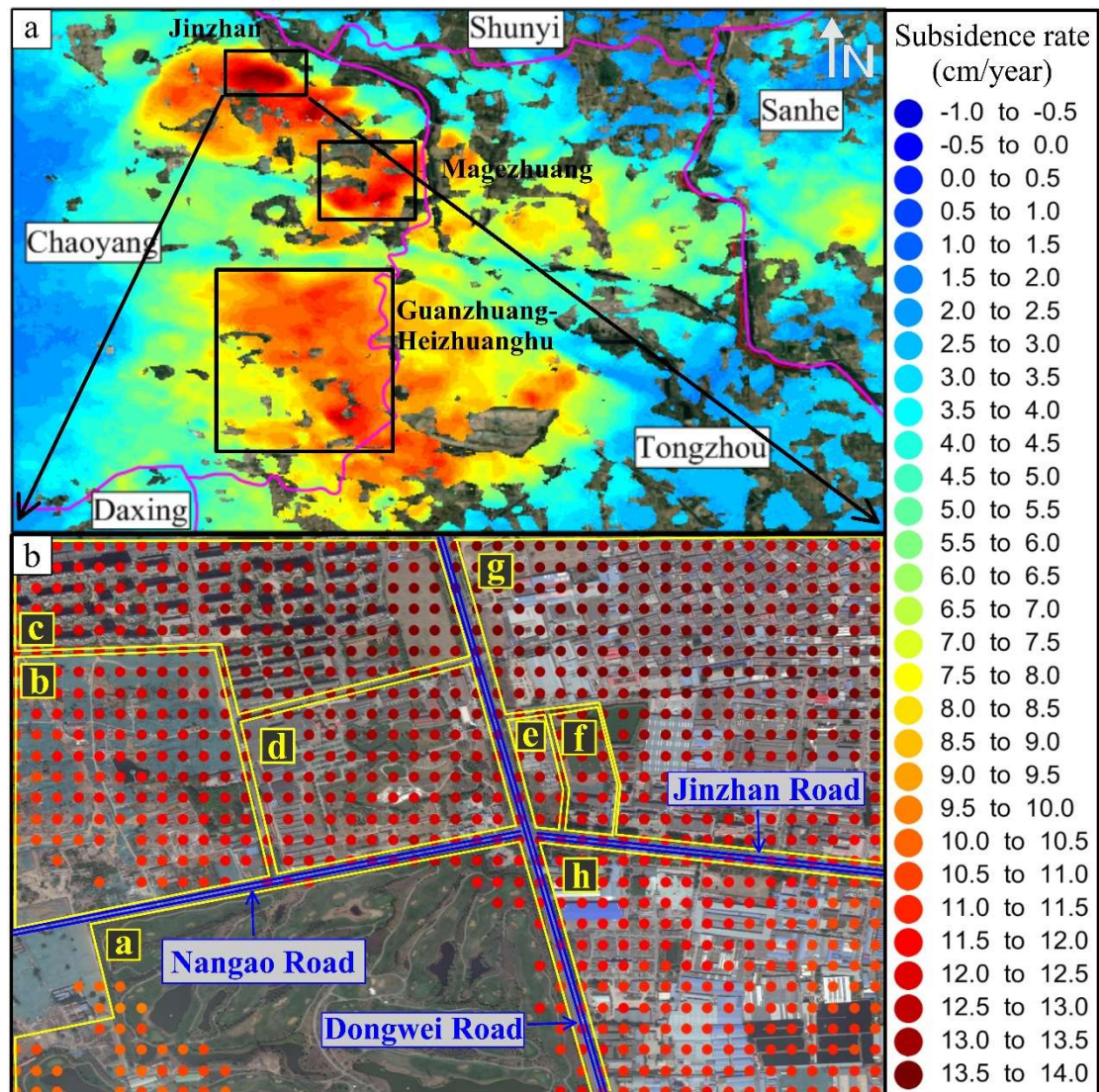
Fig. 7. (a) Enlarged maps of the three eastern subsidence bowls (i.e. rectangle b in Fig. 4); (b) Land use classification in the zone of maximum land subsidence of Jinzhan area.

To explore the land use of the subsidence center in Jinzhan area, an enlarged map of the subsidence rate (superimposed onto the high-resolution optical image obtained from Google Earth) was created as shown in Fig. 7b. Dongwei Road is a main road in this area from north to south while Nangao Road and Jinzhan Road cross this area from west to east. A detailed land use classification report is shown in Fig. 7b. In the southwest corner of this area, there are no coherent points due to the existence of vegetation and this place is (a) Tian'an Holiday Golf Club. In the north of this area, another holiday village is located here, namely (d) Tulip hot spring holiday village. Area (b) is waiting to be developed. All the places need large amounts of groundwater to ensure the water supply. Area (c) is a residential area, including several housing estates. In the east of this area, there are a large number of commercial buildings and

residential buildings (g) (h). Area (f) is Beijing Jinzhan primary school and area (e) is Xingang Huizhong motor sales company, both located near the intersection of the two roads. This area presents an elevated subsidence potential due to the presence of high thickness of compressible fine grain sediments (Chen et al., 2016). However, it is clear in Fig. 7b that the subsidence near (a) is actually lower than (g) and (c), which are the commercial buildings and residential buildings area. It was speculated that the load transmitted to the soil by the high density of commercial and high-rise residential buildings, and the high demand for groundwater from the two entertainment clubs, may also have contributed to the severe land subsidence in this area. This hypothesis is apparently supported by the fact that the increase of land subsidence towards the NE agrees with the direction of decline of the hydraulic head elevation in 2015 in this area plotted by Zhou et al. (2018).

## 5 Relationship between faults and land subsidence
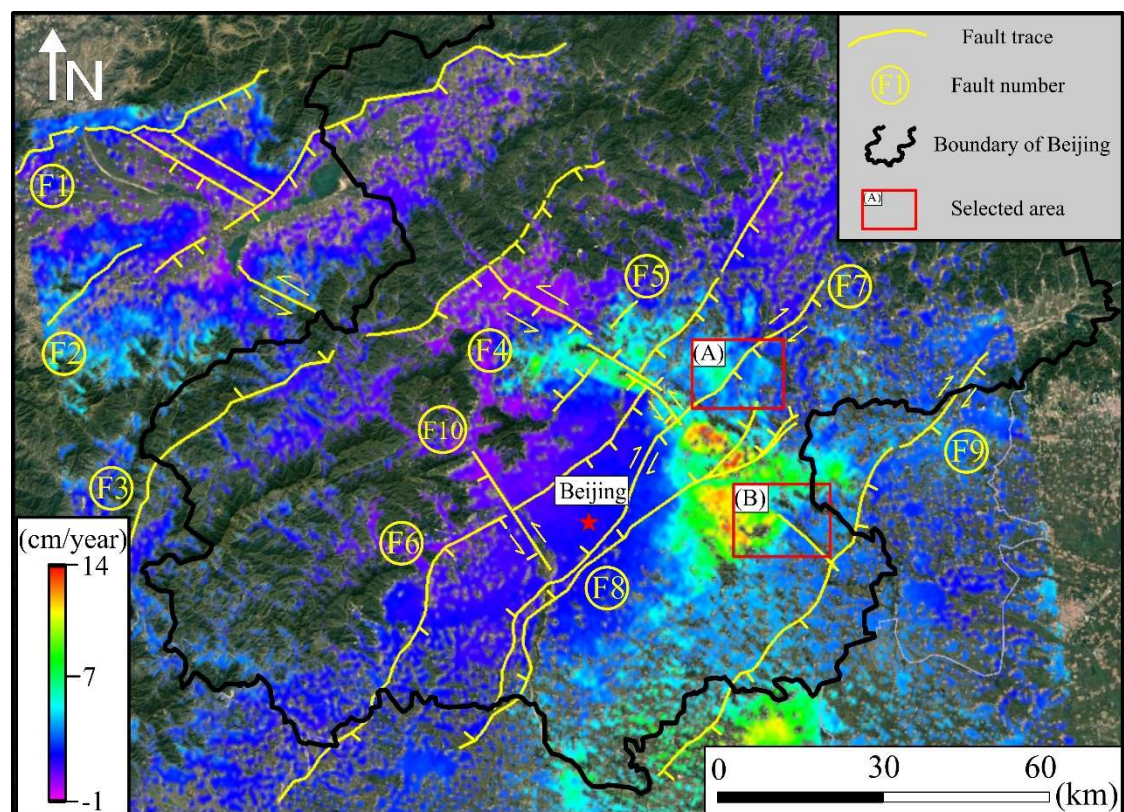
Fig. 8. Geological faults and land subsidence map in the Beijing main urban area. (A) and (B) are the selected areas analyzed in detail in the main text.

The subsidence map in Beijing shows a strip-like pattern with several linear boundaries clearly observable, especially in north-eastern Beijing, which may indicate potential links between the land subsidence and the geological faults described in

section 2.1. In Fig. 8, 7 faults (i.e. F4-F10) located in the Beijing main urban area, are plotted within the subsidence map. It is clear that some of these linear boundaries correspond to active fault traces (the projections of faults onto the ground surface), especially for the Nankou-Sunhe fault (F4) and Shunyi-Liangxiang fault (F7), indicating the existence of a spatial control of land subsidence. At both sides of these normal faults, clear land subsidence differences can be recognized.

In particular, in the east of the Shunyi-Liangxiang fault, the location of the fault trace is close to the subsidence boundary, which suggests that there is a relationship between them in this area (as shown in Fig. 8a). Beijing Capital International Airport is located at this location. We conducted further detailed analysis and the results are shown in Fig. 9.
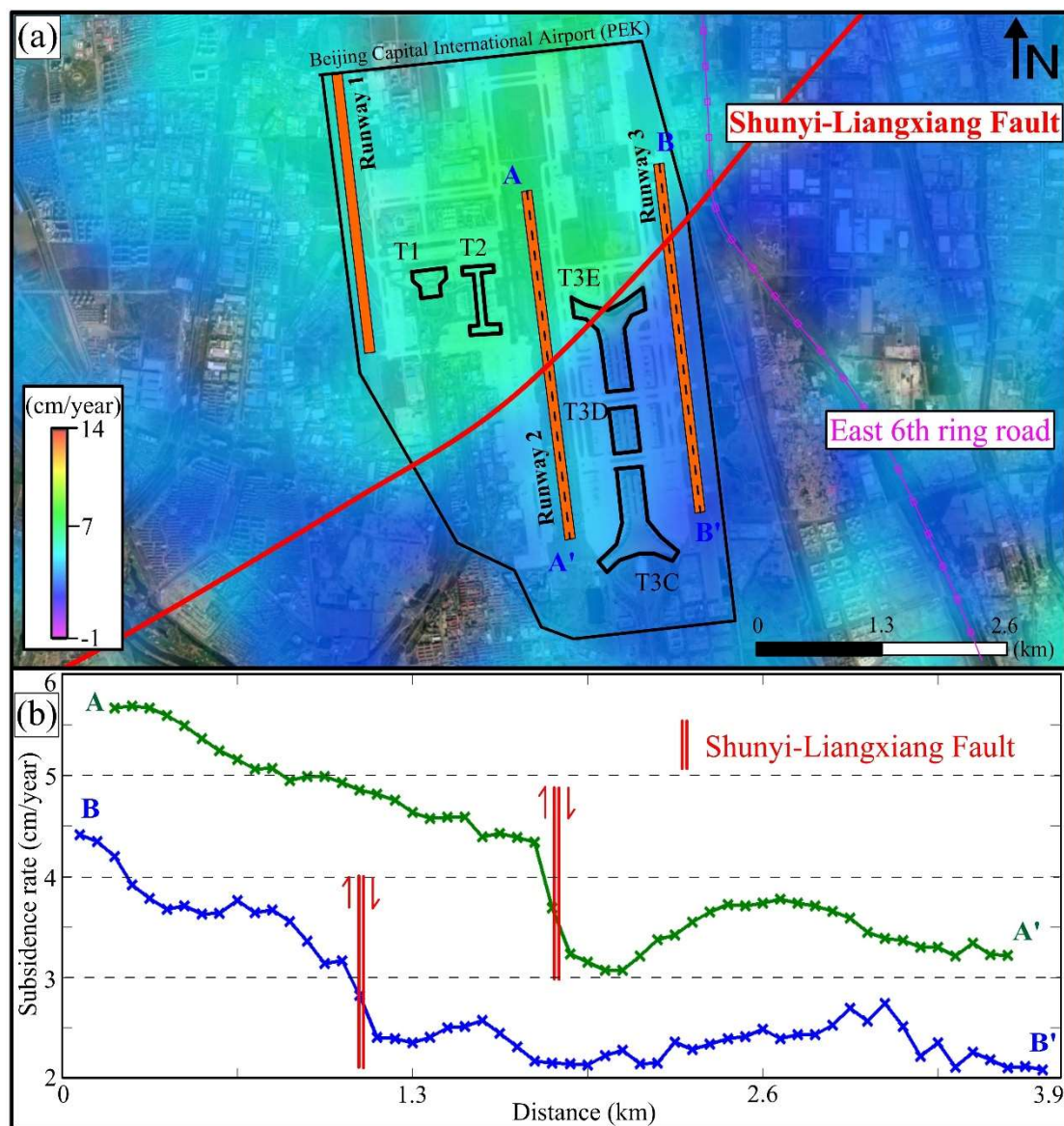

Fig. 9. (a) Subsidence map and fault location covering PEK airport (rectangular box A

in Fig. 8); (b) Land subsidence profiles along runway 2 and 3.

The subsidence map of Beijing Capital International Airport (PEK) is shown in Fig. 9a. Terminals 1 and 2 are labeled as T1 and T2, respectively. Terminal 3 (labeled as T3), opened in 2008 with 336,000 m^2 (Airports-China, 2014), was the second largest airport terminal in the world, including a main passenger terminal (Terminal 3C, T3C) and two satellite concourses (Terminals 3D and 3E, T3D and T3E). The three runways are marked with orange lines and all of them are longer than 3 km. The third runway (runway 3) was opened in 2007 to relieve the congestion of the other two runways.
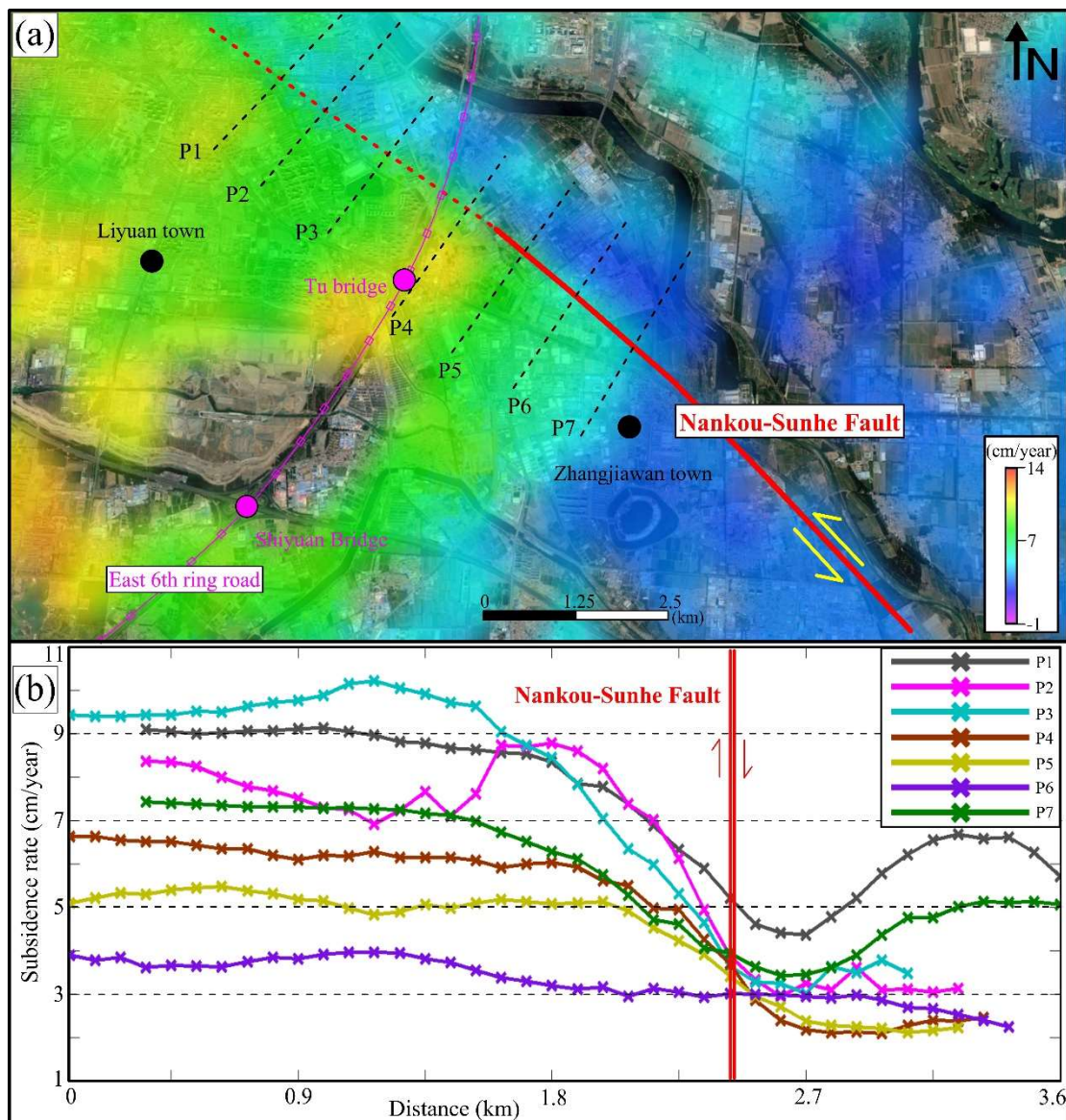

Fig. 10. (a) Land subsidence map and fault location covering the rectangular box B in Fig. 8; (b) Land subsidence profiles along P1 to P7.

It can be seen from Fig. 9a that Shunyi-Liangxiang Fault (the red line) traverses

the whole airport and cuts the airport into two parts, while in the subsidence map, there are two parts clearly presenting different subsidence rate divided by the fault trace. The arrows in the top of the fault symbol in Fig. 9b indicate the relative displacement of the fault. In the west of the fault trace, the west airport part presented relative severe subsidence with a maximum rate of 7 cm/year, while in the east of the fault trace, the east of the airport presents a relatively uniform and stable subsidence, with a rate of around 2 cm/year. This subsidence results show a good agreement with the results derived from the recent study (Gao et al., 2016) during the period from 2003 to 2013. We can see clearly significant different subsidence rates on both sides of the fault (Fig. 9b), which indicates that the fault is active. Consequently, it is crucial to closely monitor these runways in the long run towards future mitigation and emergence action plans.

The area in Fig. 8b including the east part of the Nankou-Sunhe fault is shown in Fig. 10. From the subsidence pattern, a near-linear boundary can be seen along the fault trace. Seven profiles (i.e. profiles P1-P7) traverse the fault (red line) and its extension lines are drawn. As a result, the subsidence along these 7 profiles are shown in Fig. 10b. It is clear that in the west of the Nankou-Sunhe Fault (including its extension line), land subsidence is relatively severe with a subsidence rate of 5 to 10 cm/year. In the east of the Nankou-Sunhe Fault, the land subsidence has changed from 2 to 5 cm/year, highlighting the fault trace influence on land subsidence. The profile P1-P4 traversed the extension line of the fault, but the boundary is clear, indicating the existence of a blind fault. It should be noted that actually we attempted to analyze all faults. However, for the faults 1 to 3, the coherent points with subsidence rate did not cover the two sides of fault due to decoherence caused by the vegetation in the Yanshan mountainous, north-west of Beijing. For the faults 5-6 and fault 8-10, we attempted to draw the profile as Fig. 9 and Fig. 10. However, the results showed that there were no clear fault-dependent differential difference along these faults.

From these two cases, as shown in Fig. 9 and Fig. 10, it can be derived that; a) land subsidence has dramatically changed at the locations of the Shunyi-Liangxiang and Nankou-Sunhe faults; b) the fault trace is a clear sign of the subsidence change; c) the location of faults has a clear effect on the spatial distribution of land subsidence probably due to (e.g. Holzer and Pampeyan, 1981; Burbey, 2002) the abrupt discontinuity in horizontal hydraulic conductivity related to the structure of the

basement and the differential vertical compaction of heterogeneous thicknesses of compressible soil deposited at both sides of the faults (higher in the hanging wall in normal faults). This observed structural control of land subsidence produces uneven subsidence rates on each side of the fault trace that could affect urban infrastructures (e.g. roads, railways, etc.), causing damage; d) InSAR has demonstrated to be an efficient method to map these faults which should be considered for future urban planning, and for involvement in technical solutions to avoid infrastructure damage due to differential subsidence and; e) finally, continuous monitoring of these areas is required to update the information regarding the kinematics of these faults, and to detect critical situations capable of causing damage on urban infrastructures placed on these areas.

6 Conclusion

In this paper, the land subsidence in Beijing during the period of 2015-2017 was investigated by applying time series InSAR techniques using Sentinel-1 SAR data sets with 22 SAR images and 108 interferograms providing sufficient observation for the accurate results.

The results show that the area of Beijing is still experiencing severe subsidence with a maximum rate of 140 mm/year, which corresponds to data derived from previous study, e.g. 110 mm/year in 2003~2010 (Chen et al., 2016) and 146 mm/year in 2010~2015 (Zhou et al., 2017). Additionally, these results show a good agreement with the displacement data derived from 12 GPS stations located in Beijing. The mean difference and standard deviation of the difference were -1.9 and 3.6 mm/year, respectively. Three main subsiding bowls exhibiting subsistence of more than 10 cm/year were identified in the east of Beijing, namely; Jinzhan, Magezhuang and Guanzhuang-Heizhuanghu. Therefore, for the subsidence mitigation, priority attention should be paid to these areas.

In the land subsidence map, several patterns exhibiting near-linear boundaries were found. We derived the exact location, direction, late Quaternary activity of the main potential active faults in Beijing by our three years project. We analyzed the link between the location of these subsidence boundaries and the geological fault traces. By the profile comparisons generated, it was apparent that there are some clear correlations between the distribution of faults and land subsidence, e.g. Nankou-Sunhe fault (F4) and Shunyi-Liangxiang fault (F7).

To summarize, this paper revealed that (i) the present (2015~2017) land subsidence in Beijing is still severe with a maximum subsidence rate of 14 cm/year; (ii) As the present subsidence in Beijing is mainly caused by the over-extraction of groundwater (Zhu et al. 2015; Chen et al. 2016; Chen et al. 2019), the subsidence pattern is spatially controlled by the geological faults to some degree, causing uneven subsidence that could affect infrastructures. Therefore, the continuous update of these maps is recommended to anticipate critical situations and adopt mitigation measures if required.

Acknowledgments

Reference

Airports-China, Beijing Capital International Airport. http://www.airports-china.com/beijing-zbaa-pek.htm (Accessed 14 May, 2018)

Berger, M.; Aschbacher, J., 2012. Preface: The sentinel missions—new opportunities for science. Remote Sensing of Environment, 120, 1-2.

Bos, M.S., Fernandes, R.M.S., Williams, S.D.P., and Bastos, L., 2013. Fast Error Analysis of Continuous GNSS Observations with Missing Data. J. Geod., Vol 87(4), 351-360, doi:10.1007/s00190-012-0605-0.

Burbey, T., 2002. The influence of faults in basin-fill deposits on land subsidence, Las

Vegas Valley, Nevada, USA. Hydrogeology Journal, 10(5), 525-538.

Chen, B., Gong, H., Lei, K., Li, J., Zhou, C., Gao, M., Guan, H., Lv, W., 2019. Land subsidence lagging quantification in the main exploration aquifer layers in Beijing plain, China. International Journal of Applied Earth Observation and Geoinformation, 75, 54-67.

Chen, B., Gong, H., Li, X., Lei, K., Gao, M., Zhou, C., Ke, Y., 2015. Spatial–temporal evolution patterns of land subsidence with different situation of space utilization. Natural Hazards 77, 1765-1783.

Chen, B., Gong, H., Li, X., Lei, K., Zhu, L., Gao, M., Zhou, C., 2017. Characterization and causes of land subsidence in Beijing, China. International Journal of Remote Sensing 38, 808-826.

Chen, C., Zebker, H, 2002. Phase unwrapping for large SAR interferograms: statistical segmentation and generalized network models. Geoscience and Remote Sensing, IEEE Transactions on 40, 1709-1719.

Chen, M., Tomás, R., Li, Z., Motagh, M., Li, T., Hu, L., Gong, H., Li, X., Yu, J., Gong, X., 2016. Imaging Land Subsidence Induced by Groundwater Extraction in Beijing (China) Using Satellite Radar Interferometry. Remote Sensing 8, 468.

Crosetto, M., Monserrat, O., Cuevas-González, M., Devanthéry, N., Crippa, B., 2015. Persistent Scatterer Interferometry: A review. ISPRS Journal of Photogrammetry and Remote Sensing.

Dai, K., Li, Z., Tomás, R., Liu, G., Yu, B., Wang, X., Cheng, H., Chen, J., Stockamp, J., 2016. Monitoring activity at the Daguangbao mega-landslide (China) using Sentinel-1 TOPS time series interferometry. Remote Sensing of Environment 186, 501-513.

Dai, K., Liu, G., Li, Z., Li, T., Yu, B., Wang, X., Singleton, A., 2015. Extracting Vertical Displacement Rates in Shanghai (China) with Multi-Platform SAR Images. Remote Sensing 7, 9542-9562.

Deng, Q., Zhang, P., Ran, Y., Yang, X., Min, W., Chu, Q., 2003. Basic characteristics of active tectonics of China. Science in China 46, 356-372.

Deng, Z., Ke, Y., Gong, H., Li, X., Li, Z., 2017. Land subsidence prediction in Beijing based on PS-InSAR technique and improved Grey-Markov model. GIScience & Remote Sensing, 1-22.

Ding, X. L., Li, Z. W., Zhu, J. J., Feng, G. C., & Long, J. P., 2008. Atmospheric effects on InSAR measurements and their mitigation. Sensors, 8(9), 5426-5448.

Du, Z.; Ge, L.; Ng, A.H.-M.; Xiaojing, L.; Li, L., 2018. Mapping land subsidence over the eastern beijing city using satellite radar interferometry. International Journal of Digital Earth, 11, 504-519.

ESA, Sentinel-1. https://earth.esa.int/web/guest/missions/esa-operational-eo-missions/sentinel-1 (Accessed on 14 May, 2018a)

ESA, Level-1, https://sentinel.esa.int/web/sentinel/user-guides/sentinel-1-sar/product-types-processing-levels/level-1 (Accessed on 13 November, 2018b)

GAMMA REMOTE SENSING, 2018. https://www.gamma-rs.ch/gamma.html (Accessed on 16 November, 2018)

Gao, M., Gong, H., Chen, B., Li, X., Zhou, C., Shi, M., Si, Y., Chen, Z., Duan, G., 2018. Regional Land Subsidence Analysis in Eastern Beijing Plain by InSAR Time Series and Wavelet Transforms. Remote Sensing 10, 365.

Gao, M., Gong, H., Chen, B., Zhou, C., Chen, W., Liang, Y., Shi, M., Si, Y., 2016. InSAR time-series investigation of long-term ground displacement at Beijing Capital International Airport, China. Tectonophysics.

Geudtner, D., Prats, P., Yague, N., Navas-Traver, I., Barat, I., & Torres, R., 2016. Sentinel-1 SAR Interferometry Performance Verification. In EUSAR 2016: 11th European Conference on Synthetic Aperture Radar, Proceedings of (pp. 1-4). VDE.

GMV innovating solutions, 2017. Sentinels POD Product handbook. (Avialiable at : https://sentinels.copernicus.eu/documents/247904/685154/Sentinels-POD-Product-Handbook)

Goldstein, R., Werner, C., 1998. Radar interferogram filtering for geophysical applications. Geophysical Research Letters 25, 4035-4038.

Gong, H., Zhang, Y., Xiaojuan, L., 2009. The research of land subsidence in Beijing based on permanent scatterers interferometric synthetic aperture radar (PS-InSAR) technique. Progress in Natural Science 19, 1261-1266.

Hanssen, R. F. 2001. Radar interferometry: data interpretation and error analysis (Vol. 2). Springer Science & Business Media.

Hu, B., Wang, H.-S., Sun, Y.-L., Hou, J.-G., Liang, J., 2014. Long-term land subsidence monitoring of Beijing (China) using the small baseline subset (SBAS) technique. Remote Sensing 6, 3648-3661.

Holzer, T. and Pampeyan, E., 1981. Earth fissures and localized differential subsidence. Water resources research, 17(1), 223-227.

Li, F., Goldstein, R., 1990. Studies of multibaseline spaceborne interferometric synthetic aperture radars. IEEE Transactions on Geoscience and Remote Sensing 28, 88-97.

Li, Y., Zhang, J., Li, Z., Luo, Y., 2013. Land Subsidence in Beijing City from InSAR Time Series Analysis with Small Baseline Subset. Geomatics and Information Science of Wuhan University 38, 1374-1377.

Li, Z., Fielding, E., Cross, P., 2009. Integration of InSAR time-series analysis and water-vapor correction for mapping postseismic motion after the 2003 Bam (Iran) earthquake. Geoscience and Remote Sensing, IEEE Transactions on 47, 3220-3230.

Li, Z., Fielding, E. J., Cross, P., & Muller, J. P., 2006. Interferometric synthetic aperture

radar atmospheric correction: GPS topography-dependent turbulence model. Journal of Geophysical Research: Solid Earth, 111(B2).

Li, Z., Muller, J. P., Cross, P., & Fielding, E. J., 2005. Interferometric synthetic aperture radar (InSAR) atmospheric correction: GPS, Moderate Resolution Imaging Spectroradiometer (MODIS), and InSAR integration. Journal of Geophysical Research: Solid Earth, 110(B3).

Liang, F., Sun, J., Shen, Z., Xu, X., 2013. Accumulated crustal deformation and its characteristics in Beijing and surrounding regions in 2007–2010 from L-band InSAR. Earthquake 33, 43-54.

Luo, X., Wang, J., Xu, Z., Zhu, S., Meng, L., Liu, J., and Cui, Y., 2018. Dynamic analysis of urban ground subsidence in Beijing based on the permanent scattering InSAR technology. Journal of Applied Remote Sensing, 12(2), 026001.

Marinkovic, P., Larsen, Y., 2016. Subsidence of Beijing (China) mapped by Copernicus Sentinel-1 time series interferometry. Zenodo.

Motagh, M., Shamshiri, R., Haghshenas Haghighi, M., Wetzel, H.-U., Akbari, B., Nahavandchi, H., Roessner, S., Arabi, S., 2017. Quantifying groundwater exploitation induced subsidence in the Rafsanjan plain, southeastern Iran, using InSAR time-series and in situ measurements. Engineering Geology 218, 134-151.

Ng, A., Ge, L., Li, X., Zhang, K., 2012. Monitoring ground deformation in Beijing, China with persistent scatterer SAR interferometry. Journal of Geodesy 86, 375-392.

Osmanoğlu, B., Sunar, F., Wdowinski, S., Cabral-Cano, E., 2015. Time series analysis of InSAR data: Methods and trends. ISPRS Journal of Photogrammetry and Remote Sensing.

Prats, P., Marotti, L., Wollstadt, S., & Scheiber, R., 2010. Investigations on TOPS interferometry with TerraSAR-X. In Geoscience and Remote Sensing Symposium (IGARSS), 2010 IEEE International (pp. 2629-2632). IEEE.

Scheiber, R., Moreira, A., 2000. Coregistration of interferometric SAR images using spectral diversity. IEEE Transactions on Geoscience and Remote Sensing 38, 2179-2191.

Xu, X., Wu, W., Zhang, X., Ma, S., Ma, W., Yu, g., Gu, M., Jiang, W., 2002. Crust Newly Tectonic Deformation and Earthquake in Capital Zone. Beijing: Science Press.

Xu, Y., Shen, S., Cai, Z., Zhou, G., 2008. The state of land subsidence and prediction approaches due to groundwater withdrawal in China. Natural Hazards 45, 123-135.

Yague, N., Prats, P., Gonzalez, F., Brcic, R., Shau, R., Geudtner, D., Eineder, M., Bamler, R., 2016. Interferometric Processing of Sentinel-1 TOPS Data. IEEE Transactions on Geoscience and Remote Sensing.

Yang, G., Han, Y. and Wang, M., 2003. Characteristics of the horizontal crustal

movement of North China in the last decade. Earthquake Research in China 19(4): 324-333.

Yang, Q., Ke, Y., Zhang, D., Chen, B., Gong, H., Lv, M., Zhu, L., and Li, X., 2018. Multi-Scale Analysis of the Relationship between Land Subsidence and Buildings: A Case Study in an Eastern Beijing Urban Area Using the PS-InSAR Technique. Remote Sensing, 10(7), 1006.

Yu, C., Li, Z., Penna, N. T., & Crippa, P., 2018. Generic atmospheric correction model for Interferometric Synthetic Aperture Radar observations. Journal of Geophysical Research: Solid Earth, 123(10), 9202-9222.

Yu, C., Li, Z., & Penna, N. T., 2018. Interferometric synthetic aperture radar atmospheric correction using a GPS-based iterative tropospheric decomposition model. Remote Sensing of Environment, 204, 109-121.

Zhang, Y., Gong, H., Gu, Z., Wang, R., Li, X. and Zhao, W., 2014. Characterization of land subsidence induced by groundwater withdrawals in the plain of beijing city, china. Hydrogeology Journal 22: 397-409.

Zhou, C., Gong, H., Chen, B., Li, J., Gao, M., Zhu, F., Chen, W., Liang, Y., 2017. InSAR Time-Series Analysis of Land Subsidence under Different Land Use Types in the Eastern Beijing Plain, China. Remote Sensing 9, 380.

Zhou, C., Gong, H., Zhang, Y., Warner, T., Wang, C., 2018. Spatiotemporal Evolution of Land Subsidence in the Beijing Plain 2003–2015 Using Persistent Scatterer Interferometry (PSI) with Multi-Source SAR Data. Remote Sensing 10, 552.

Zhou, W., Li, S., Zhou, Z., Chang, X., 2016. Remote Sensing of Deformation of a High Concrete-Faced Rockfill Dam Using InSAR: A Study of the Shuibuya Dam, China. Remote Sensing 8, 255.

Zhu, L., Gong, H., Li, X., Wang, R., Chen, B., Dai, Z., Teatini, P., 2015. Land subsidence due to groundwater withdrawal in the northern Beijing plain, China. Engineering Geology 193, 243-255.